Mechanisms of Arsenate Adsorption by Highly-Ordered Nano-Structured Silicate Media Impregnated with Metal Oxides

ARTICLE *in* ENVIRONMENTAL SCIENCE AND TECHNOLOGY · DECEMBER 2003

Impact Factor: 5.33 · DOI: 10.1021/es0343712 · Source: PubMed

4 AUTHORS, INCLUDING:

Min Jang
University of Malaya
63 PUBLICATIONS **816** CITATIONS
SEE PROFILE

Jae Park
University of Wisconsin–Madison
47 PUBLICATIONS **1,406** CITATIONS
SEE PROFILE

Sang Il Choi
Seoul National University Bundang Hospital
166 PUBLICATIONS **2,650** CITATIONS
SEE PROFILE

Environ. Sci. Technol. **2003**, *37,* 5062−5070

Mechanisms of Arsenate Adsorption by Highly-Ordered Nano-Structured Silicate Media Impregnated with Metal Oxides

MIN JANG,[§] EUN WOO SHIN,[†] JAE KWANG PARK,*[,§] AND SANG IL CHOI[‡]

Department of Civil and Environmental Engineering, University of Wisconsin—Madison, 1415 Engineering Drive, Madison, Wisconsin 53706, Forest Products Laboratory, USDA, One Gifford Pinchot Drive, Madison, Wisconsin 53705, and Department of Environmental Engineering, Kwangwoon University, 447-1 Wolgye-Dong Nowon-Gu, Seoul, Korea

The highly ordered mesoporous silica media, SBA-15, was synthesized and incorporated with iron, aluminum, and zinc oxides using an incipient wetness impregnation technique. Adsorption capacities and *kinetics* of metal-impregnated SBA-15 were compared with activated alumina which is widely used for arsenic removal. Media impregnated with 10% of aluminum by weight (designated to Al_{10}SBA-15) had 1.9−2.7 times greater arsenate adsorption capacities in a wide range of initial arsenate concentrations and a 15 times greater initial sorption rate at pH 7.2 than activated alumina. By employing one- and two-site models, surface complexation modeling was conducted to investigate the relationship between the aluminum oxidation states in different media and adsorption behaviors shown by adsorption *isotherms* and *kinetics* since the oxidation phase of aluminum incorporated onto the surface of SBA-15 was Al−O, which has a lower oxidation state than activated alumina (Al_2O_3). Surface complexation modeling results for arsenate adsorption edges conducted with different pH indicated that the monodentate complex ($SAsO_4^{2-}$) was dominant in Al_{10}SBA-15, while bidentate complexes ($XHAsO_4$ and $XAsO_4^-$) were dominant in activated alumina at pH 7.2, respectively. In *kinetic* studies at pH 7.2 ± 0.02, Al_{10}SBA-15 had only a fast-rate step of initial adsorption, while activated alumina had fast- and slow-rate steps of arsenate adsorption. Therefore, it can be inferred that the monodentate arsenate complex, predominant in Al_{10}SBA-15, leads to faster adsorption rates than bidentate arsenate complexes favored with activated alumina. An arsenate adsorption behavior and arsenate surface complexation were thought to be well explained by aluminum oxidation states and surface structural properties of media.

Introduction

Throughout the world, arsenic is creating potentially serious environmental problems for humans and other living organisms. Most reported arsenic problems are found in groundwater water supply systems and are caused by natural processes such as mineral weathering and dissolution caused by the changes of geochemical environments to reductive conditions (*1, 2*). Arsenic contamination is also caused by human activities such as mining wastes, petroleum refining, sewage sludge, agricultural chemicals, ceramic manufacturing industries, and coal fly ash (*3*−*5*).

Small public water systems will face heavy financial burdens in order to comply with new stringent regulations which will lower the arsenic contamination limit from 50 to 10 ppb (*6*). Because of this, a highly effective, reliable, and economic technique is needed to meet the new arsenic maximum contaminant level. Many adsorbents have been developed as a promising technology for arsenic removal due to their easiness of set up (*2, 7*−*15*). For the POE/POU (Point of Entry/Point of Use) adsorption system, activated alumina has been one of the best available adsorbents and has been extensively studied because of its effectiveness and selectiveness for arsenic adsorption removal (*7, 16*). However, the highly alkaline feeding solution should be controlled with an acidic solution to have a pH between 5.5 and 6.0 so that optimum arsenic adsorption capacity of activated alumina can be achieved (*17*). When activated alumina was regenerated, its adsorption capacity was reported to be reduced by 30−40% (*18*). Furthermore, due to the slower adsorption reaction, activated alumina requires relatively longer empty bed contact times (3−5 min) than ion-exchange resins (*19*).

The M41S family of mesoporous silicate molecular sieves, developed in 1992, has opened up new possibilities in the fields of catalysis, sensors, and adsorbents (*20*). These materials are synthesized with a self-assembled molecular array of surfactant molecules as a structure-directing template, which results in very sharp and ordered pore distributions of inorganic materials as well as a high surface area and pore volume. These materials can be classified by pore structures as follows: MCM-41 (two-dimensional hexagonal mesopore structure), MCM-48 (three-dimensional cubic mesopore structure), and MCM-50 (lamellar mesopore structure). The newly developed mesoporous silica molecular sieve SBA-15 was successfully synthesized using amphiphilic triblock copolymers as a structure-directing template agent under hydrothermal conditions. It has uniform two-dimensional hexagonal (space group *p6mm*) mesopore channels that can be tailored by changing synthesis conditions (*21*). Compared with the M41S types, the mesoporous silica SBA-15 molecular sieve has a higher hydrothermal stability and larger pore sizes (about 50−100 Å) without pore expanding chemicals; therefore, it can likely incorporate a large portion of the metal precursor without blocking effects (*21*). In addition, water or ethanol extraction can be applied to recover the pore-forming template for reuse in SBA-15 synthesis due to the weak interaction between two-dimensional hexagonal silica and triblock copolymer mesophases (*22*). SBA-15 has a surface area of 600−1000 m^2/g and a pore volume of 0.6−1.3 cm^3/g which provide highly active sites for applications to adsorption, catalysis, or sensors (*23*). Through several incorporation techniques, the organic or inorganic materials can be functionalized onto the monolayer of highly ordered nano-structured materials. Figure 1 shows the schematic of the proposed structure of the aluminum impregnated SBA-15. Due to their advanced characteristics, the incorporation of functioning materials for mesoporous materials have so far been spotlighted in terms of synthesis, mechanism, and application (*22, 24*−*26*).

In this study, the relationship between the type of surface complexation and the rate of adsorption was investigated

* Corresponding author phone: (608)262-7247; fax: (608)262-5199; e-mail: park@engr.wisc.edu.
[†] Forest Products Laboratory.
[‡] Kwangwoon University.
[§] University of Wisconsin—Madison.

10.1021/es0343712 CCC: $25.00
Published on Web 10/09/2003

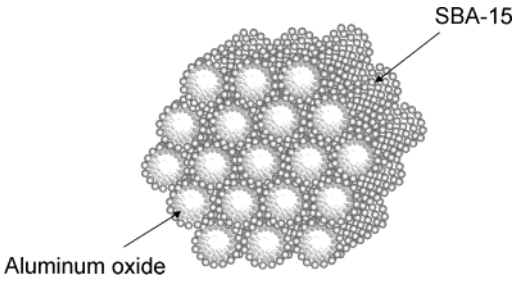

FIGURE 1. Schematic of the proposed structure of the aluminum impregnated SBA-15.

with surface complexation modeling using the constant capacitance model (CCM) for aluminum-impregnated SBA-15 and activated alumina. Because of the unavailability of the extended X-ray absorption fine structure (EXAFS) spectroscopy that can be directly used for experimental investigation of the surface complex structures (*27*), the identity of the complex was ascertained by modeling of the arsenate adsorption edges. In our surface complexation modeling, the oxidation states of metal in the media were modeled with two different site species [monodentate (SOH) and bidentate ($X(OH)_2$)], since our previous results of X-ray photoelectron spectroscopy (XPS) study showed that the oxidation phase of aluminum impregnated SBA-15 was assigned to Al−O which is a lower oxidation state than that of activated alumina (Al_2O_3) (*28*).

The objectives of this study were as follows: (1) to produce adsorbents by synthesizing highly ordered mesoporous silica SBA-15 and incorporating metal oxides onto the SBA-15 surface by use of an incipient-wetness impregnation technique; (2) to evaluate the adsorption of arsenate species onto metal oxide incorporated mesoporous silica; and (3) to investigate the arsenate adsorption behavior of new adsorbents employing the one- and two-site models in surface complexation modeling using CCM.

Methodology

Synthesis of Metal Oxide Impregnated SBA-15. SBA-15 was synthesized using a triblock copolymer (Pluronic P123, EO_{20}-$PO_{70}EO_{20}$, Aldrich) as a structure-directing reagent and tetraethyl orthosilicate (Aldrich) as a silica precursor. Four grams of the triblock copolymer was dissolved in 60 mL of deionized water for 30 min, and a 2 M hydrochloric acid solution was added. The mixed solution was stirred for 30 min. Tetraethyl orthosilicate (TEOS) was then added to the mixture, and the mixture was heated at 35 °C for 20 h. The mixture was transferred into a Teflon bottle and heated at 80 °C for 24 h without stirring. The solid product was then filtered from the mixture with a 0.45-μm filter and dried at room temperature under vacuum before calcination. The mole fraction of each component for as-synthesized SBA-15 was 1 mol TEOS:5.854 mol HCl:162.681 mol H_2O:0.0168 mol triblock copolymer. Calcination was performed in an oven at 550 °C for 6 h in air to remove the triblock copolymer organic component. The calcined SBA-15 was preserved at room temperature under vacuum. $Al(NO_3)_3 \cdot 9H_2O$, $Fe(NO_3)_3 \cdot 9H_2O$, and $Zn(NO_3)_2 \cdot 6H_2O$ were selected as aluminum, iron, and zinc precursors, respectively, to incorporate metals into SBA-15 through use of an incipient wetness impregnation technique. Each metal precursor was dissolved in the deionized water at given concentrations. The 10% of aluminum impregnated SBA-15 (weight of aluminum/weight of SBA-15) was designated as Al_{10}SBA-15. The mixture was dried in a hood at room temperature for 1 day. All solids were then calcined in an oven programmed to increase the temperature from room temperature to 400 °C at a rate of 0.5 °C per minute, and then hold the temperature for 4 h. After calcination, the solids were kept inside a vacuum chamber. After synthesizing the media, the conductivity tests were performed to confirm the complete oxidation of the aluminum precursor. Each 0.02 g of media was stirred with 5 mL of deionized water for 10 min and filtered out with a 0.45-μm filter. The conductivity of the filtrate was analyzed with a conductance meter (YSI model 32). The conductivities were below 10 μS/cm, which is the same as that of deionized water, indicating no leaching of aluminum ions.

Characterization of Media. X-ray diffraction (XRD) patterns were obtained using a Stoe High-Resolution X-ray Diffractometer (Microphotonics, Allentown, PA) equipped with CuKα radiation (40 kV, 25 mA) with a 0.05° step size and 5 s step time over the range $0.8° < 2\theta < 6.0°$. N_2 gas adsorption *isotherms* were performed at 77 K using a Micromeritics ASAP 2000 analyzer (Norcross, GA). Media were dehydrated at 250 °C for 1 day before performing *isotherm* tests. The BET specific surface area was calculated using the linear portion of the BET equation. The pore size distributions of media were obtained using Barrett, Joyner, and Halenda (BJH) analysis (*29*) of the desorption branch of the hysteresis loop of the nitrogen adsorption *isotherm*. The pore diameter (D_{BJH}), mesopore surface area (A_{BJH}), and volume (V_{BJH}) were calculated from the pore size distribution curve. The pore diameter (D_{BJH}) was calculated using the following equation:

$$D_{BJH} = 4V_{BJH}/A_{BJH} \quad (1)$$

Arsenate Adsorption *Isotherm* Tests. Sodium arsenate ($Na_2HAsO_4 \cdot 7H_2O$, Sigma) was used as the arsenate source without any modification. A stock solution of arsenate was prepared at a concentration of 133 mmol/L in deionized water prepared with a Photronix reagent grade water system. $NaNO_3$ (0.01 M) solution prepared with deionized water was poured into a polyethylene bottle of a predetermined volume. Then, a small volume of arsenic stock solution was added to achieve the target arsenate concentration and pH was adjusted with a pH automatic titrator (Model 48pH 1/16 DIN pH controller, EXTECH), using small volumes of acid (HNO_3, 0.1 M) and base (NaOH, 0.1 M) solutions. All samples were mixed in a rotary shaker at 250 rpm and 25 ± 0.5 °C. After 8 h of shaking, the pH of the samples was readjusted with the automatic pH titrator. All samples were then shaken again in the rotary shaker until equilibrium was reached. After 24 h of shaking, 5 mL was withdrawn and filtered with a 0.45-μm Uniflo filter unit. All data of the arsenic adsorption *isotherm* were fitted with *Freundlich* and *Langmuir isotherm* models. The *Langmuir isotherm* is expressed as follows

$$q_{eq} = \frac{bQ_{max}C_{eq}}{1 + bC_{eq}} \quad (2)$$

where Q_{max} (mmol/g) is the maximum adsorption capacity corresponding to complete monolayer coverage, C_{eq} (mmol/L) is the equilibrium solute concentration, and b is the equilibrium constant related to the energy of sorption (L/mmol).

The *Freundlich isotherm* model was also tested to describe the adsorption data. It assumes that different sites are involved with several adsorption energies (*30*). The *Freundlich isotherm* is expressed as follows:

$$q_{eq} = KC_{eq}^{1/n} \quad (3)$$

A nonlinear least-squares regression analysis was applied to obtain all *Langmuir* and *Freundlich isotherm* parameters.

Arsenate and Other Metal Ions Analysis. Arsenate was analyzed with an Inductively Coupled Plasma Atomic Emission Spectrometer (ULTIMA, Jobin Yvon Inc., Edison, NJ) for samples which were set up with initial arsenate concentra-

TABLE 1. Surface Complexation Reactions and Intrinsic Surface Complexation Constants in a Constant Capacitance Model (CCM) for Arsenate Adsorption

reactions	equilibrium expressions
Surface Hydrolysis Reactions for Monodentate Hydroxyl Groups	
(1) $SOH^a + H^+ \leftrightarrow SOH_2^+$	$K_{S+}(\text{int}) = \frac{[SOH_2^+]}{[SOH][H^+]}\exp\left(\frac{F\Psi_0}{RT}\right)$
(2) $SOH \leftrightarrow SO^- + H^+$	$K_{S-}(\text{int}) = \frac{[SO^-][H^+]}{[SOH]}\exp\left(-\frac{F\Psi_0}{RT}\right)$
Surface Hydrolysis Reactions for Bidentate Hydroxyl Groups	
(3) $X(OH)_2{}^b + H^+ \leftrightarrow HOXOH_2^+$	$K_{X+}(\text{int}) = \frac{[HOXOH_2^+]}{[X(OH)_2][H^+]}\exp\left(\frac{F\Psi_0}{RT}\right)$
(4) $X(OH)_2 \leftrightarrow HOXO^- + H^+$	$K_{X-}(\text{int}) = \frac{[HOXO^-][H^+]}{[XOH]}\exp\left(-\frac{F\Psi_0}{RT}\right)$
Monodentate Arsenate Adsorption Reactions	
(5) $SOH + H_3AsO_4 \leftrightarrow SH_2AsO_4 + H_2O$	$K_{SAs(V)}{}^1(\text{int}) = \frac{[SH_2AsO_4]}{[SOH][H_3AsO_4]}$
(6) $SOH + H_3AsO_4 \leftrightarrow SHAsO_4^- + H^+ + H_2O$	$K_{SAs(V)}{}^2(\text{int}) = \frac{[SHAsO_4^-][H^+]}{[SOH][H_3AsO_4]}\exp\left(-\frac{F\Psi_0}{RT}\right)$
(7) $SOH + H_3AsO_4 \leftrightarrow SAsO_4^{2-} + 2H^+ + H_2O$	$K_{SAs(V)}{}^3(\text{int}) = \frac{[SAsO_4^{2-}][H^+]^2}{[SOH][H_3AsO_4]}\exp\left(-2\frac{F\Psi_0}{RT}\right)$
Bidentate Arsenate Adsorption Reactions	
(8) $X(OH)_2 + H_3AsO_4 \leftrightarrow XHAsO_4 + 2H_2O$	$K_{XAs(V)}{}^1(\text{int}) = \frac{[XHAsO_4]}{[X(OH)_2][H_3AsO_4]}$
(9) $X(OH)_2 + H_3AsO_4 \leftrightarrow XAsO_4^- + H^+ + 2H_2O$	$K_{XAs(V)}{}^2(\text{int}) = \frac{[XAsO_4^-][H^+]}{[X(OH)_2][H_3AsO_4]}\exp\left(-\frac{F\Psi_0}{RT}\right)$

[a] One reactive surface hydroxyl group bound to a surface metal ion S. [b] Two reactive surface hydroxyl group bound to a surface metal ion X which is topologically and geometrically distinct from metal ion S (*33*).

tions greater than 0.133 mmol/L. A Varian AA-975 Atomic Absorption Spectrophotometer and a GTA-95 Graphite Tube Atomizer with programmable sample dispenser (Palo Alto, CA) were used for samples set up with arsenate concentrations lower than 0.133 mmol/L. In this analysis, 20 mg/L of nickel solution was used as a matrix modifier. The detection limits of ICP-AES and AAS-graphite were 2.5 and 0.0474 μg/L for arsenic, respectively.

Potentiometric Titration. To determine two surface hydrolysis constants, potentiometric titration tests were conducted with activated alumina and Al_{10}SBA-15. Before testing, all solids were carefully washed with deionized water and dried under vacuum for 1 day. Solid samples were then added to 200 mL of 0.01 M $NaNO_3$ solution with a suspension concentration of 1 g/L. Suspensions were equilibrated for 1 h to obtain stable initial pH values. After measuring the initial pH value, suspensions were titrated with 5−10 μL of 0.1 M HNO_3. Due to pH dreft, free H^+ ion concentrations were measured with a pH meter 10 min after the addition of acid using a pH meter.

Surface Complexation Modeling of Arsenate Adsorption Data. X-ray absorption fine structure (XAFS) and FTIR spectroscopic studies have recently provided evidence for the formation of inner-sphere adsorption complexes of oxyanions on hydrous ferric oxide surfaces (*5, 31*). Because of this, arsenic adsorption behaviors of various solids were investigated using the constant capacitance model (CCM) in the intrinsic surface complexation modeling (*27, 32, 33*). Arsenate adsorption *isotherm* data on Al_{10}SBA-15 and activated alumina under various pH conditions were used for surface complexation modeling. This model is based on the assumptions that (1) ion adsorption occurs through an inner-sphere ligand exchange mechanism, (2) no complexes are formed with ions of the background electrolyte, and (3) the net surface charge σ_o (mol/L) is a linear function of the surface potential ψ_o (volts) which can be represented as follows

$$\sigma_o = (CS_A M_V/F)\Psi_o \quad (4)$$

where C (F/m^2) is the capacitance density at the surface and is fixed at 1.06 (*34*), S_A (m^2/g) is the specific surface area, M_V (g/L) is the suspension density of the solid, and F (9.65 × 10^{-4} coulombs/mol) is the Faraday constant. The computer program FITEQL 4.0 (*35*) was used to optimize the intrinsic surface complexation constants and reactive surface site densities.

In this study, one- and two-site adsorption models were employed to obtain the arsenate intrinsic surface complexation constants and reactive surface site densities. The surface reaction and equilibrium expression for intrinsic surface complexation of arsenate adsorption on the media are summarized in Table 1. For the one-site adsorption model, monodentate mononuclear adsorption of arsenate was described by reactions 5−7, including the surface protonation

and deprotonation reactions 1 and 2 in Table 1. For the two-site adsorption model, the reactions 7−9 represent the monodentate and bidentate mononuclear adsorption reactions, respectively, while reactions 1−4 were used as surface protonation and deprotonation reactions for both monodentate and bidentate surface hydroxyls. To optimize the intrinsic surface complexation constants and hydroxyl densities for each model, the sequential optimization strategy was applied. Two surface protonation and deprotonation reaction constants [$K_{S/X+}$(int) and $K_{S/X-}$(int)] were determined by fitting the data of potentiometric titration using the CCM model. However, since the surface protonation and deprotonation reaction constants can be changed by the surface hydroxyl density, a value of surface hydroxyl density was inserted into the model to obtain the surface hydrolysis constants through fitting potentiometric titration data. These surface hydrolysis constants were used as fixed values for the one-site model in which the intrinsic surface complexation constants [$K_{SAs(V)}{}^1$(int), $K_{SAs(V)}{}^2$(int), and $K_{SAs(V)}{}^3$(int)] and total monodentate hydroxyl site density (SOH) were obtained by optimizing the arsenate adsorption data. If the obtained surface hydroxyl density value was different from the one obtained from fitting the potentiometric titration data, the above process was repeated until the difference between surface hydroxyl density values for potentiometric titration and arsenate adsorption edge data was within 1%. Through this approach, it was possible to achieve the best fit for both potentiometric titration and arsenate adsorption experimental data simultaneously. For the two-site model, the equilibrium constants of bidentate adsorption [$K_{XAs(V)}{}^1$(int) and $K_{XAs(V)}{}^2$(int)] and two different hydroxyl sites [SOH and $X(OH)_2$] were optimized by holding the surface protonation and deprotonation constants and $K_{SAs(V)}{}^3$(int) (monodentate adsorption) as fixed values in the CCM model. In this model, two different hydroxyl sites can be assumed to be topologically and geometrically distinct (*33*). In addition, it can be assumed that protonation of surface hydroxyls would favor the bidentate adsorption at a low pH (*4, 33*). To optimize two different hydroxyl site densities, the total hydroxyl sites (SOH) determined from the one-site model was set equal to the total hydroxyl site densities as follows:

$$(SOH)_{ONE-SITE} = (SOH)_{TWO-SITE} + (X(OH)_2)_{TWO-SITE} \quad (5)$$

Based on the values of the weighted sum of squares divided by the degrees of freedom (WSOS/DF) calculated in FITEQL 4.0, the optimized ratio between monodentate and bidentate hydroxyl densities and the intrinsic surface complexation constants were determined.

Arsenate Adsorption *Kinetics*. The arsenate stock solution was prepared following the same procedure described for the adsorption *isotherm* tests. An aliquot of 300 mL of deionized water was prepared with 0.01 M $NaNO_3$ and poured into a reaction bottle for each *kinetic* study. After injecting a small volume of arsenate stock solution to make the desired arsenate concentration, the suspension was stirred with the magnetic stirrer at a velocity of 500 rpm. The pH of the solution was adjusted with an automatic titrator, and the temperature was maintained at 25 ± 0.5 °C for 1 h before the adsorbent was injected at a predetermined mass. To maintain a constant pH during *kinetic* studies, the automatic titrator was installed in the reactor and connected to a pH electrode and small tubes running from two pumps that could titrate with small volumes of an acid (HNO_3, 0.1 M) and a base (NaOH, 0.1 M) stock solution. One of the two pumps, connected to either the acid or the base stock solution, was operated when the pH drifted by ± 0.02 pH units from the initial pH. An aliquot of 3 mL of suspension was withdrawn at 2−60 min intervals and filtered through a 0.45-μm Uniflo filter unit for arsenate analysis. Activated alumina (Aldrich)

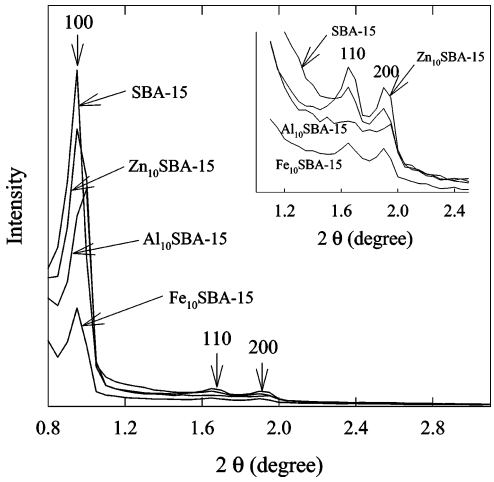

FIGURE 2. X-ray diffraction patterns for calcined SBA-15 and 10 wt % aluminum, iron, and zinc-impregnated SBA-15.

was selected to compare the adsorption *isotherm* and *kinetic* data with aluminum-impregnated SBA-15. The surface area and the average pore diameter of activated alumina were 155 m^2/g and 5.9 nm, respectively. For many adsorption processes using heterogeneous materials, it was found that the pseudo-second-order *kinetic* equation agrees with chemisorption as the rate-controlling step (*30, 36*). Therefore, all *kinetic* data were fitted with a pseudo-second-order *kinetic* model to estimate the rate constants, initial sorption rates, and adsorption capacities for arsenate.

The pseudo-second-order *kinetic* model can be solved with the following equations. The *kinetic* rate equation is expressed as (*30, 36−38*)

$$\frac{dq_t}{dt} = k_2(q_{eq} - q_t)^2 \quad (6)$$

where q_{eq} is the sorption capacity at equilibrium, q_t is the solid-phase loading of arsenate at time t, and t is time (min). The k_2 ($g \cdot mmol^{-1} \cdot min^{-1}$) is the pseudo-second-order rate constant for the kinetic model. By integrating eq 4 with the boundary conditions of $q_t = 0$ (at $t = 0$) and $q_t = q_t$ (at $t = t$), the following linear equation can be obtained:

$$\frac{t}{q_t} = \frac{1}{v_0} + \frac{1}{q_{eq}}t \quad (7)$$

$$v_0 = k_2 \cdot q_{eq}{}^2 \quad (8)$$

where v_0 ($mmol\ g^{-1} \cdot min^{-1}$) is the initial sorption rate. Therefore, the v_0 and q_{eq} values of *kinetic* tests can be determined experimentally by plotting t versus t/q_t.

Results and Discussion

X-ray Diffraction. X-ray diffraction results are shown in Figure 2. Calcined SBA-15 displayed a well-resolved pattern with a sharp peak at 0.95° and two weak peaks at 1.65° and 1.90°. This X-ray diffraction pattern was similar to that reported for SBA-15 (*21*). The XRD peaks can be indexed to a hexagonal lattice with a d_{100} spacing (the d spacing value for the intense (100) peak) of 92.91 Å, corresponding to a large unit cell parameter, a_0, of 107.3 Å obtained by the following equation: $a_0 = 2 \times d_{100}/\sqrt{3}$. The intensities of peaks decreased for samples incorporated with 10% of each metal by weight. The decreases in peak intensities were in the following order: Fe > Al > Zn. Although periodicities of pore structures decreased for all solid samples, 10% of each metal by weight was incorporated without creating complete

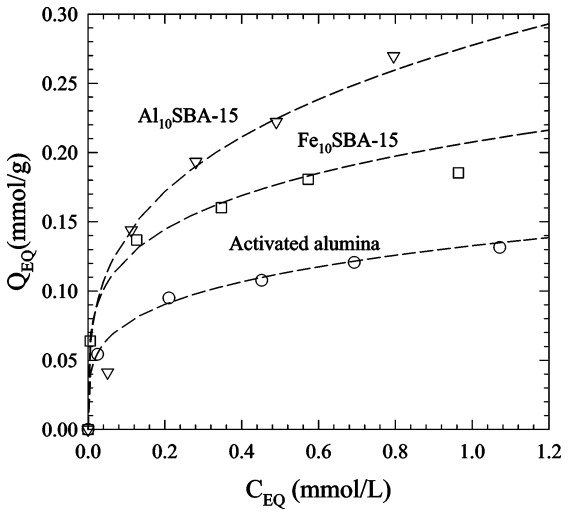

FIGURE 3. Arsenate adsorption *isotherms* for activated alumina, Al_{10}SBA-15, and Fe_{10}SBA-15 (temperature = 25 ± 0.5 °C, $NaNO_3$ (ionic strength) = 0.01 M, and pH = 6.55 ± 0.02). The curves were obtained from *Freundlich isotherms*.

TABLE 2. Arsenate Adsorption *Isotherms* at Different Arsenate Initial Concentrations Ranging from 0.133 to 1.33 mmol/L for Activated Alumina, Al_{10}SBA-15, and Fe_{10}SBA-15[a]

adsorption *isotherms* and parameters	activated alumina	Al_{10}SBA-15	Fe_{10}SBA-15
Langmuir			
b (L/mmol)	32.8	8.9	108.1
Q_{max} (mmol/g)	0.12	0.28	0.17
R^2	0.971	0.966	0.980
Freundlich			
K ($mmol^{1-1/n}\cdot L^{1/n}/g$)	0.13	0.28	0.21
n	0.24	0.30	0.23
R^2	0.995	0.996	0.995

[a] Determination coefficients (R^2) and parameters for the fit of arsenate adsorption *isotherm* data to both *Freundlich* and *Langmuir isotherms*.

clogging of the pore structures. All peak positions of Al_{10}-SBA-15 were shifted to have smaller d_{100} (88.27 Å) and a_0 (101.9 Å), which correspond to a lattice contraction of about 5%, respectively. This result might be caused by partial substitution of silicon by aluminum and incorporation of aluminum oxide onto mesopore structures (*39*).

Arsenate Adsorption *Isotherm*. Figure 3 shows the arsenate adsorption *isotherm* results at pH 6.55 ± 0.02 for all adsorbents at different initial arsenate concentrations ranging from 0.133 to 1.33 mmol/L. The solution volume and suspension concentration were 50 mL and 2 g/L, respectively. Arsenate was adsorbed on Fe_{10}SBA-15 and Al_{10}SBA-15 in greater amounts than activated alumina. However, Zn_{10}SBA-15 did not have a good arsenate adsorption capacity, showing below 0.03 $mmol_{As}$/g for all equilibrium data. SBA-15 incorporated with 10% of aluminum had 2.36 times greater maximum adsorption capacity (Q_{max}) than activated alumina (Table 2). At the initial arsenate concentration of 1.33 $mmol_{As}$/L, the observed arsenate adsorption densities of each metal compound were 0.0067 $mmol_{As}/mmol_{Al}$ (activated alumina), 0.073 $mmol_{As}/mmol_{Al}$ (Al_{10}SBA-15), 0.103 $mmol_{As}/mmol_{Fe}$ (Fe_{10}SBA-15), and 0.012 $mmol_{As}/mmol_{Zn}$ (Zn_{10}SBA-15). Based on the mole fraction of arsenate and each metal, Al_{10}SBA-15 and Fe_{10}SBA-15 had 10.9 and 15.4 times greater arsenate adsorption densities than activated alumina, respectively. Equilibrium adsorption data of all samples were fit with two different *isotherm* models—*Langmuir* and *Freundlich*. The results are summarized in Table 2. With the exception of Zn_{10}SBA-15, which had an R^2 value of 0.741, all data fit very

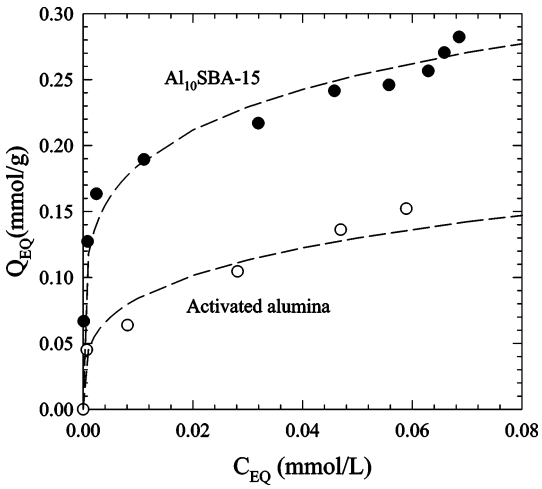

FIGURE 4. Arsenate adsorption *isotherms* of activated alumina and Al_{10}SBA-15 performed at the initial arsenate concentration of 0.133 mmol/L (temperature = 25 ± 0.5 °C, $NaNO_3$ (ionic strength = 0.01 M, and pH = 6.55 ± 0.02). The curves were obtained from *Freundlich isotherms*.

TABLE 3. Arsenate Adsorption *Isotherms* of Activated Alumina and Al_{10}SBA-15 Performed at the Initial Arsenate Concentration of 0.133 mmol/L[a]

adsorption *isotherms* and parameters	activated alumina	Al_{10}SBA-15
Langmuir		
b (L/mmol)	1049.9	3518.8
Q_{max} (mmol/g)	0.11	0.22
R^2	0.765	0.933
Freundlich		
K ($mmol^{1-1/n}\cdot L^{1/n}/g$)	0.29	0.46
n	0.27	0.20
R^2	0.924	0.960

[a] Determination coefficients (R^2) and parameters for the fit of arsenate adsorption *isotherm* data to both *Freundlich* and *Langmuir isotherms*.

well with the *Freundlich isotherm* model, as indicated by R^2 values of >0.99. The other metal compounds such as iron, aluminum, and zinc ions were not detected in solution by ICP-AES.

Figure 4 shows the arsenate adsorption *isotherms* of Al_{10}-SBA-15 and activated alumina performed at the initial arsenate concentration of 0.133 mmol/L. For this *isotherm*, the aliquot volume was 100 mL, and masses of both adsorbents were varied. The final pH was fixed at 6.55 ± 0.02. Arsenate adsorption capacities of Al_{10}SBA-15 increased to 0.19, 0.247, and 0.26 $mmol_{As}$/g, while activated alumina increased to 0.075, 0.125, and 0.135 $mmol_{As}$/g at 0.01, 0.04, and 0.06 mmol/L of arsenate equilibrium concentrations, respectively. Under a broad range of equilibrium arsenate concentrations below 0.1 mmol/L, Al_{10}SBA-15 showed about 1.9−2.7 times greater adsorption capacities than activated alumina. The fitting parameters and determination coefficient (R^2) values for activated alumina and Al_{10}SBA-15 are summarized in Table 3. As in the previous *isotherm* fitting results, the *Freundlich isotherm* provided a better fit than the *Langmuir isotherm*. Thus, as seen in the arsenate adsorption capabilities of a broad range of arsenate concentration, it can be concluded that Al_{10}SBA-15 can achieve a higher efficiency of arsenate adsorption for arsenate concentrations of 300 ppb.

Nitrogen Adsorption−Desorption *Isotherm*. The N_2 adsorption−desorption *isotherms* of SBA-15 and Al_{10}SBA-15 are shown in Figure 5(A). When 10% of aluminum was

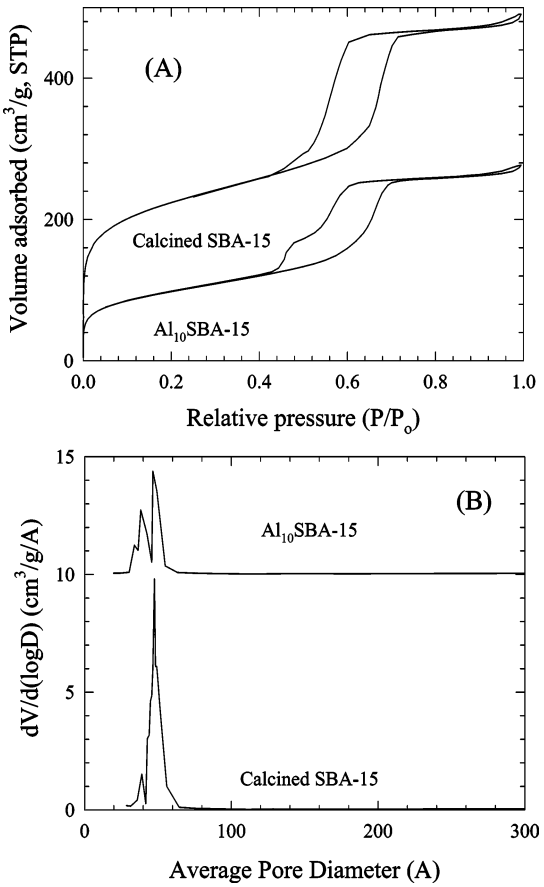

FIGURE 5. (A) N_2 Adsorption/desorption *isotherms* of nitrogen at 77 K for calcined SBA-15 and Al_{10}SBA-15 and (B) pore size distribution obtained by d*V*/d(logD) according to average pore diameter.

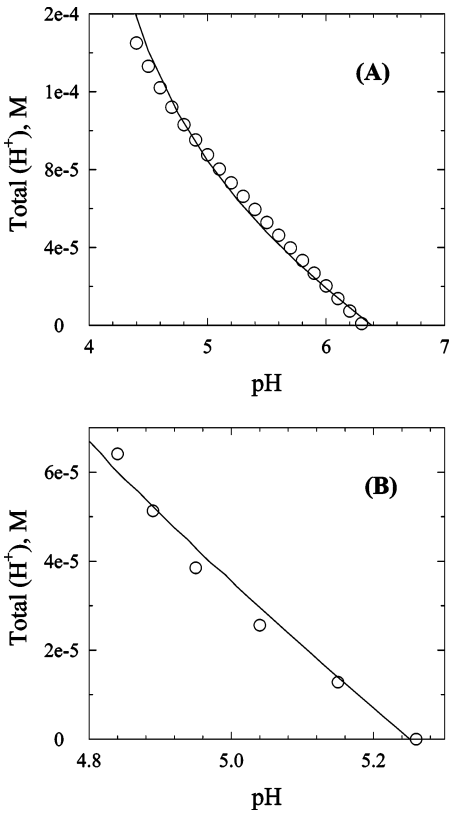

FIGURE 6. Potentiometric titration of (A) activated alumina and (B) Al_{10}SBA-15.

incorporated by weight into SBA-15, the sharpness of the inflection was significantly reduced at the P/P_o range from 0.4 to 0.8, and the inflections were shifted slightly toward lower P/P_o ranges. The inflection point of the relative pressure is related to a diameter in the mesopore range, and the sharpness of these steps indicates the uniformity of the mesopore size distribution (*25, 40*). Compared to SBA-15, Al_{10}SBA-15 showed a reduction of sharpness, indicating less uniformity of mesopore size distribution. Parameters of pore structure for calcined SBA-15 and Al_{10}SBA-15 were calculated from the desorption branch of the nitrogen *isotherm* using the BJH formula (*29*). The A_{BET}, A_{BJH}, V_{BJH}, and D_{BJH} values for calcined SBA-15 were 768.1 m^2/g, 554.6 m^2/g, 0.66 cm^3/g, and 47.9 Å, respectively, and 343.1 m^2/g, 412.5 m^2/g, 0.45 cm^3/g, and 43.2 Å for Al_{10}SBA-15, respectively. Therefore, all parameters of Al_{10}SBA-15 decreased compared with SBA-15. The reduction of surface area, pore size, and pore volume indicated the formation of aluminum oxides within pore structures (*23*). Figure 5(B) shows the pore size distribution curves of calcined SBA-15 and Al_{10}SBA-15 obtained from desorption *isotherm* branches and the BJH formula. As shown in Figure 5(B), the calcined SBA-15 showed a very sharp pore size distribution obtained by d*V*/d(logD) ($cm^3/g/Å$) according to the average pore diameter. The pore size distribution of Al_{10}SBA-15, however, showed a bimodal shape, in which a smaller mesopore distribution was produced. The bimodal pore distribution of Al_{10}SBA-15 seemed to be caused by heterogeneity of incipient wetness impregnation, which is very similar to the result of Luan et al. (*40*).

Potentiometric Titration and Surface Complexation Modeling. Figure 6 shows the results and calculated lines of potentiometric titration experiments for both activated alumina and Al_{10}SBA-15. The solid lines represent the calculated data at a solid suspension concentration of 1 g/L and an ionic strength of 0.01 M. The surface hydrolysis constants and hydroxyl densities were optimized with the procedure described previously so as to satisfy both potentiometric titration and arsenate adsorption *isotherm* data simultaneously. The numerical input values, surface hydrolysis constants, intrinsic surface complexation constants, and surface hydroxyl densities of both one- and two-site assumptions optimized by CCM are summarized in Table 4 as well as the WSOS/DF (weighted sum of squares divided by degrees of freedom) values of each optimization. The WSOS/DF values fitted to the potentiometric titration data for both activated alumina and Al_{10}SBA-15 are less than 20, which represent reasonably good fitting results (*35*). Al_{10}-SBA-15 had lower surface protonation and deprotonation constants than activated alumina. This result could be caused by the mixed effect of the mesoporous silicate surface which was not covered by aluminum oxides. This was supported by pore size distribution analysis obtained from N_2 gas *isotherm*. The point of zero charge (PZC) values for silica are typically below pH 3 due to permanent structural negative charge (*4*). The result of optimization showed that the surface hydroxyl density of Al_{10}SBA-15 (1.68×10^{-6} mol/m^2) was approximately 2.2 times greater than activated alumina (0.78×10^{-6} mol/m^2). This suggests that a higher reactive surface site density could be achieved by dispersing active metal oxides onto the mesoporous silicate supporter even if aluminum oxide is not homogeneously incorporated on the surface of SBA-15. The surface hydrolysis constants and surface hydroxyl densities obtained from the above optimization procedure were therefore used as fixed values for obtaining the intrinsic surface complexation constants for the one- and two-site models.

Figure 7 shows the adsorption edge data of activated alumina and Al_{10}SBA-15 at different pH values at equilibrium as well as calculated lines of surface complexes obtained from the one-site model. The solid and dashed lines represent

TABLE 4. Numerical Input Values and Intrinsic Surface Complexation Constants of the Surface Acidity, One-Site (Monodentate Adsorption) and Two-Site (Mono- and Bidentate Adsorption) Assumption of Arsenate

experiments or assumption	parameters	activated alumina	Al_{10}SBA-15
potentiometric titration	suspension density (g/L)	1	1
	surface area (m^2/g)	155	412.5
	site density (mol/m^2)	0.78×10^{-6}	1.68×10^{-6}
	site density (mol/L)	1.21×10^{-4}	6.912×10^{-4}
	Log $K_{X/S+}$ (int)	6.24	4.11
	Log $K_{X/S-}$ (int)	−6.37	−6.29
	WSOS/DF	12.9	2.90
one-site assumption	suspension density (g/L)	0.5	0.25
	Log $K_{SAs(V)}{}^1$ (int)	9.94	7.21
	Log $K_{SAs(V)}{}^2$ (int)	1.13	2.75
	Log $K_{SAs(V)}{}^3$ (int)	−2.52	−1.95
	SOH (monodentate hydroxyl density, mol/L)	5.84×10^{-5}	1.508×10^{-4}
	WSOS/DF	9.02	1.73
two-site assumption	Log $K_{SAs(V)}{}^3$ (int)	−2.52	−1.95
	Log $K_{XAs(V)}{}^1$ (int)	13.56	8.08
	Log $K_{XAs(V)}{}^2$ (int)	7.03	3.10
	SOH (monodentate hydroxyl density, mol/L)	2.07×10^{-5}	8.50×10^{-5}
	$X(OH)_2$ (bidentate hydroxyl density, mol/L)	3.77×10^{-5}	6.58×10^{-5}
	ratio (SOH/$X(OH)_2$)	0.549	1.29
	WSOS/DF	19.68	19.62

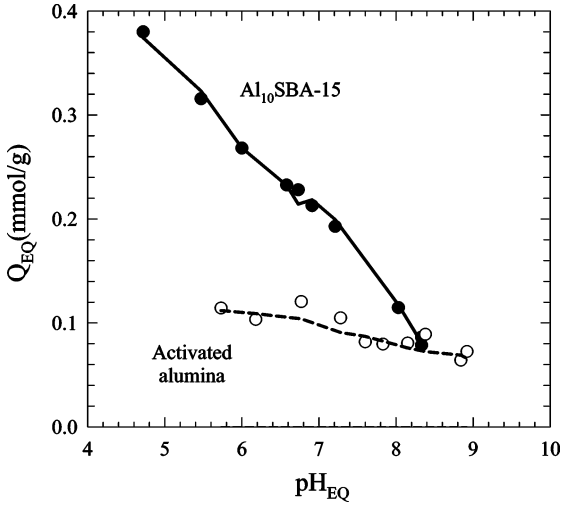

FIGURE 7. Adsorption edges of activated alumina (○) and Al_{10}-SBA-15 (●) under different pH conditions at equilibrium state.

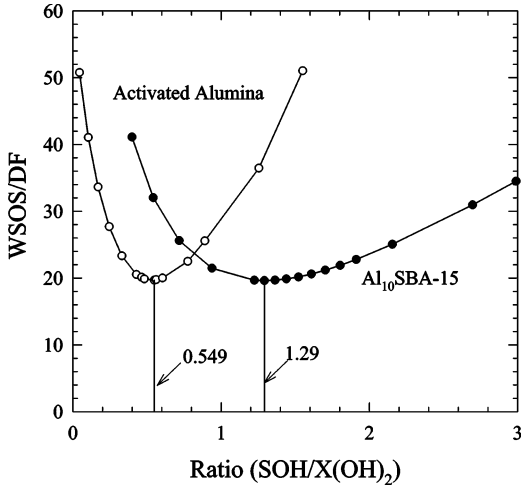

FIGURE 8. WSOS/DF values determined by optimization of two-site model according to the ratio between monodentate and bidentate hydroxyl densities.

the fitted lines for Al_{10}SBA-15 and activated alumina optimized by the one-site model (monodentate adsorption), respectively. Arsenate adsorption capacities of Al_{10}SBA-15 increased linearly with decreasing pH, while activated alumina did not show significant changes in adsorption capacities with changes in pH. When the best fits were obtained with the one-site model, the WSOS/DF values were 9.02 and 1.73 for both activated alumina and Al_{10}SBA-15, respectively, showing fairly reasonable fitting (Table 4). At pH 6.5 of the calculated fitting lines, Al_{10}SBA-15 (0.23 $mmol_{As}$/g) had approximately 2.1 times greater adsorption capacity than activated alumina (0.11 $mmol_{As}$/g). This result was in agreement with previous *isotherm* tests performed with 0.133 $mmol_{As}$/L of arsenate initial concentration. The adsorption tendency of Al_{10}SBA-15 at different pH conditions at equilibrium was very similar, although its adsorption capacities were much greater than other studies, in which oxyanion adsorption on goethite was investigated (*5, 31*).

Figure 8 shows the WSOS/DF values according to the ratio between the monodentate and bidentate hydroxyl densities for the two-site model. The minimum value of WSOS/DF represents the best fit. The optimized ratio of SOH/$X(OH)_2$ for Al_{10}SBA-15 and activated alumina are 1.29 and 0.549, respectively, and have WSOS/DF values below 20, indicating reasonably good fits. Thus, it can be concluded that Al_{10}-SBA-15 has a higher portion of monodentate hydroxyl density than activated alumina. In our other study of the binding energy of Al 2p by use of XPS analysis, the aluminum phase of Al_{10}SBA-15 was found to have lower oxidation states than that of activated alumina (*28*). Consequently, our modeling results show that the differences in the optimized ratio between monodentate and bidentate hydroxyl densities for activated alumina and Al_{10}SBA-15 agree reasonably well with the experimental result of XPS. Figure 9 shows the surface complexation species and calculated fitting lines of the two-site model for activated alumina and Al_{10}SBA-15 calculated by CCM. The solid and dashed lines represent the various surface complexes for Al_{10}SBA-15 and activated alumina. As shown in Figure 9, Al_{10}SBA-15 had the prevalent monodentate complexation species ($SAsO_4{}^{2-}$) and bidentate complexation species ($XHAsO_4$) in the pH range 6−8 and below pH 6, respectively. In the case of activated alumina, however, bidentate adsorption was predominant in a broad pH range. Therefore, it can be surmised that these different speciation trends result from the different ratio between monodentate and bidentate surface hydroxyl densities of adsorbents.

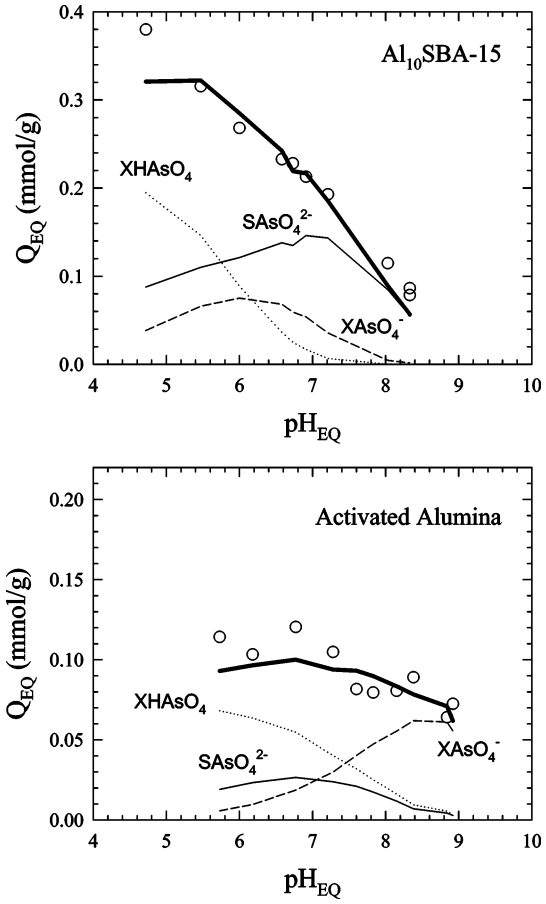

FIGURE 9. The bold solid and dashed lines represent the calculated fitting lines for Al_{10}SBA-15 and activated alumina optimized by the two-site model (the mono- and bidentate adsorption), respectively.

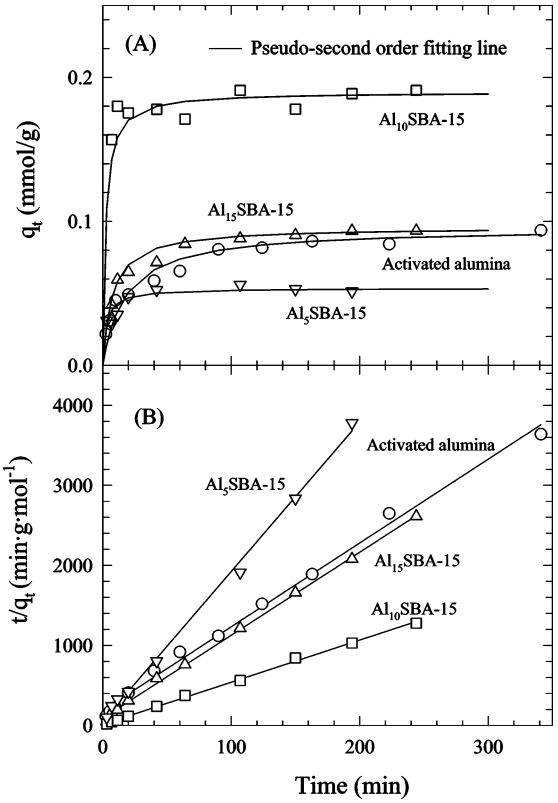

FIGURE 10. (A) Kinetics of arsenate adsorption at pH 7.2 ± 0.02, arsenate initial concentration of 0.133 mmol/L, and solid concentration of 0.333 g/L and (B) transformation with *t* (*x* axis) and *t*/q_t (*y* axis)

Kinetic Studies of Arsenic Adsorption. Figure 10(A) shows the arsenate adsorption *kinetic* data of activated alumina, Al_5SBA-15, Al_{10}SBA-15, and Al_{15}SBA-15 as well as their fitting lines of the pseudo-second-order *kinetic* model. Figure 10(B) is the plot of t versus t/q_t to determine the v_0 and q_{eq} values for all media. Table 5 shows the determination coefficients (R^2) and several parameters obtained from the pseudo-second-order *kinetic* model. The pseudo-second-order model fits closely with *kinetic* data of aluminum-impregnated SBA-15 and activated alumina, showing very high determination coefficients of above 0.99. From the *kinetic* results, Al_{10}SBA-15 had twice the adsorption capacity of activated alumina, which is consistent with previous adsorption *isotherm* tests. Al_5SBA-15 had lower adsorption capacity (in $mmol_{As}/g$) than activated alumina, while Al_{15}SBA-15 had slightly higher adsorption capacity than activated alumina but much lower than Al_{10}SBA-15. The most efficient percentage of aluminum impregnation, therefore, is 10% in terms of adsorption velocity and capacity. In the comparison of q_{eq} ($mmol_{As}/mmol_{Al}$), Al_{10}SBA-15 showed almost 10.5 times higher adsorption capacity than activated alumina. Therefore, it can be concluded that the nanoscale dispersion of aluminum oxides in the mesopore structures creates a large number of active sites for arsenate adsorption. Compared with activated alumina, Al_{10}SBA-15 had a very fast arsenate adsorption rate, in which about 94% of arsenate coverage was saturated in 12 min. However, it was observed that the arsenate adsorption *kinetic*s of activated alumina was fast for about 10 min (48% of arsenate coverage) and slow for 80 min (86% of arsenate coverage) before equilibrium was reached. The initial sorption rate of Al_{10}SBA-15 (0.0824 $mmol \cdot g^{-1} \cdot min^{-1}$) was 15 times greater than that of activated alumina (0.0054 $mmol \cdot g^{-1} \cdot min^{-1}$) at 0.333 g/L solid concentration. This fast sorption ability can be attributed to both the physical and chemical properties of aluminum-impregnated SBA-15. In terms of physical properties, aluminum-impregnated SBA-15 has hexagonal open-pore structures of the MCM-41 types, which has a relatively uniform mesopore size excluding macropore structures. Activated alumina has amorphous matrices of aluminum oxides containing bottleneck shapes of pore structures, which can hinder the accessibility of arsenate molecules to the active sites of the media (*41*). Therefore, the accessibility and transport of arsenate species can be favorable for the open and homogeneous pore structures of aluminum-impregnated SBA-15 (*42*). It may be more reasonable to explain the arsenate adsorption behavior by comparing surface reactions of aluminum-impregnated SBA-15 and activated alumina because the pseudo-second-order *kinetic* model agreed very well with chemisorptions, which are the rate controlling step (*36*−*38*). The comparative surface reaction of arsenate adsorption on Al_{10}SBA-15 appeared to

TABLE 5. Determination Coefficients (R^2) of a Pseudo-Second-Order Kinetic Model Fitting of Arsenate Adsorption Kinetics for Activated Alumina and AlSBA-15

	parameters				
media	determination coefficients (R^2)	k_2[b]	v_0[c]	q_{eq}[d]	q_{eq}[e]
AA	0.995	0.59	0.005	0.096	0.005
5%[a]	0.997	6.60	0.019	0.054	0.029
10%	0.998	2.28	0.082	0.190	0.051
15%	0.999	1.39	0.013	0.096	0.017

[a] Aluminum 5% (w/w) impregnated SBA-15. [b] ($g \cdot mmol^{-1} \cdot min^{-1}$). [c] Initial sorption rate ($mmol \cdot g^{-1} \cdot min^{-1}$). [d] q_{eq} ($mmol_{As}/g$). [e] q_{eq}($mmol_{As}/mmol_{Al}$) were obtained by a pseudo-second-order kinetic model.

be different from activated alumina because Al_{10}SBA-15 did not have a slow step like activated alumina. The following description may provide a reasonable explanation for these different *kinetic* behaviors. Grossl et al. (*5*) proposed that two-step processes were involved in obtaining an inner-sphere surface complex. The first step is the adsorption/desorption of arsenate or chromate onto hydroxyl ligands of monodentate surfaces to form an inner-sphere monodentate surface complex, which has a rapid initial ligand exchange reaction. The second step involves a second ligand exchange reaction, which is a very slow adsorption reaction. The least-squares optimization routine in the FITEQL software did not converge on surface complexation constants when the bidentate ligand complexation was included in the one-site model (*33*), therefore, the two-site model in which both monodenate and bidentate adsorption reactions occur was used in this study. It was concluded that Al_{10}SBA-15 had the predominant monodentate arsenate complex, while activated alumina favored the bidentate complexes over the monodentate complex at pH 7.2. These results are thought to occur because of the different ratios between monodentate and bidentate hydroxyl densities, which were calculated by optimizing the arsenate edges through modeling. In addition, these results have been supported experimentally by the XPS analysis of our other research (*28*). Due to several advantages such as higher adsorption capacity and velocity, aluminum-impregnated SBA-15 appears to have good potential for applying to POE/POU arsenate removal. However, better impregnation techniques should be attempted to avoid the heterogeneity of pore structures and to enhance the surface hydroxyl density.

Acknowledgments

This research was supported by grants from the Industrial and Economic Development Research Fund (I&EDR) for University-Industry Relations of the University of Wisconsin—Madison, the Applied Research Grant of the University of Wisconsin System, and the Groundwater Research Council of the Department of Natural Resources (DNR), Wisconsin. This research was also supported in part by the Korea Ministry of Environment as "The Eco-Technopia 21 Project".

Literature Cited

(1) Le, X. C.; Yalcin, S.; Ma, M. *Environ. Sci. Technol.* **2000**, *34*, 2342−2347.
(2) Namasivayam, C.; Senthilkumar, S. *Ind. Eng. Chem. Res.* **1998**, *37*, 4816−4822.
(3) Viraraghavan, T.; Subramanian, K. S.; Aruldoss, J. A. *Water. Sci. Technol.* **1999**, *40*, 69−76.
(4) Manning, B. A.; Goldberg, S. *Environ. Sci. Technol.* **1997**, *31*, 2005−2011.
(5) Grossl, P. R.; Eick, M.; Sparks, D. L.; Goldberg, S.; Ainsworth, C. C. *Environ. Sci. Technol.* **1997**, *31*, 321−326.
(6) Woods, R. *Headquarters Press Release, Environmental News* 2001.
(7) Gilles, G. C. *Water Technol.* **2000**, *September*.
(8) Tokunaga, S.; Wasay, S. A.; Park, S. W. *Water Sci. Technol.* **1997**, *35*, 71−78.
(9) Dambies, L.; Guibal, E.; Roze, A. *Colloids Surf., A* **2000**, *170*, 19−31.
(10) Reed, B. E.; Vaughan, R.; Jiang, L. *J. Environ. Eng.* **2000**, *September*, 869−873.
(11) Baes, A. U.; Okuda, T.; Nishijima, W.; Shoto, E.; Okada, M. *Water Sci. Technol.* **1997**, *35*, 89−95.
(12) Suzuki, T. M.; Tanaka, D. A. P.; Tanco, M. A. L.; Kanesato, M.; Yokoyama, T. *J. Environ. Monit.* **2000**, *2*, 550−555.
(13) Min, J. H.; Hering, J. G. *Water Res.* **1998**, *32*, 1544−1552.
(14) Haron, M. J.; Wan Yunus, W. M. Z.; Yong, N. L.; Tokunaga, S. *Chemosphere* **1999**, *39*, 2459−2466.
(15) Manju, G. N.; Raji, C.; Anirudhan, T. S. *Water Res.* **1998**, *32*, 3062−3070.
(16) Lin, T. F.; Wu, J. K. *Water Res.* **2001**, *35*, 2049−2057.
(17) Chwirka, J. D.; Thomson, B. M.; Stomp, J. M., III *AWWA* **2000**, *92*, 79−88.
(18) Ahmed, M. F. Bangladesh University of Engineering and Technology (BUET): Dhaka, Bangladesh, 2001.
(19) Johnston, R.; Heijnen, H. Bangladesh University of Engineering and Technology: Dhaka, 2001.
(20) Kresge, C. T.; Leonowicz, M. E.; Roth, W. J.; Vartuli, J. C.; Beck, J. S. *Nature* **1992**, *359*, 710.
(21) Zhao, D.; Feng, J.; Huo, Q.; Melosh, N.; Fredrickson, G. H.; Chmelka, B. F.; Stucky, G. D. *Science* **1998**, *279*, 548−552.
(22) Kruk, M.; Jaroniec, M.; Ko, C. H.; Ryoo, R. *Chem. Mater.* **2000**, *12*, 1961−1968.
(23) Morey, M. S.; O'Brien, S.; Schwarz, S.; Stucky, G. D. *Chem. Mater.* **2000**, *12*, 898−911.
(24) Margolese, D.; Melero, J. A.; Christiansen, S. C.; Chmelka, B. F.; Stucky, G. D. *Chem. Mater.* **2000**, *12*, 2448−2459.
(25) Newalkar, B. L.; Olanrewaju, J.; Komarneni, S. *Chem. Mater.* **2001**, *13*, 552−557.
(26) Zhao, D.; Sun, J.; Li, Q.; Stucky, G. D. *Chem. Mater.* **2000**, *12*, 275−279.
(27) Fendorf, S.; Eick, M. J.; Grossl, P.; Sparks, D. L. *Environ. Sci. Technol.* **1997**, *31*, 315−320.
(28) Shin, E. W.; Han, J. S.; Jang, M.; Min, S.-H.; Park, J. K.; Rowell, R. M. Submitted to *Environ. Sci. Technol.* **2003**.
(29) Barrett, E. P.; Joyner, L. G.; Halenda, P. P. *J. Am. Chem. Soc.* **1951**, *73*, 373−380.
(30) Reddad, Z.; Gerente, C.; Andres, Y.; Le Cloirec, P. *Environ. Sci. Technol.* **2002**, *36*, 2067−2073.
(31) Manning, B. A.; Fendorf, S. E.; Goldberg, S. *Environ. Sci. Technol.* **1998**, *32*, 2383−2388.
(32) Manceau, A.; Charlet, L. *J. Colloid Interface Sci.* **1994**, *168*, 87−93.
(33) Manning, B. A.; Goldberg, S. *Soil Sci. Soc. Am. J.* **1996**, *60*, 121−131.
(34) Westall, J. C.; Hohl, H. *Adv. Colloid Interface Sci.* **1980**, *12*, 265−294.
(35) Herbelin, A. L.; Westall, J. C. Department of Chemistry, Oregon State University: Corvallis, OR, 1999.
(36) Ho, Y. S.; McKay, G. *Trans IChemE* **1998**, *76B*, 332−340.
(37) Ho, Y. S.; McKay, G. *Chemical Engineering Journal* **1998**, *70*, 115−124.
(38) Ho, Y. S.; McKay, G. *Trans. IChemE* **1998**, *76B*, 183−191.
(39) Romero, A. A.; Alba, M. D.; Klinowski, J. *J. Phys. Chem. B* **1998**, *102*, 123−128.
(40) Luan, Z.; Maes, E. M.; Van der Heide, M. A. W.; Zhao, D.; Czernuszewicz, R. S.; Keven, L. *Chem. Mater.* **1999**, *11*, 3680−3686.
(41) Kim, Y. S. *Kor. J. Mater. Res.* **2001**, *11*, 957−965.
(42) Burleigh, M. C.; Markowitz, M. A.; Spector, M. S.; Gaber, B. P. *Chem. Mater.* **2001**, *13*, 4760−4766.

Received for review April 21, 2003. Revised manuscript received August 8, 2003. Accepted August 28, 2003.

ES0343712